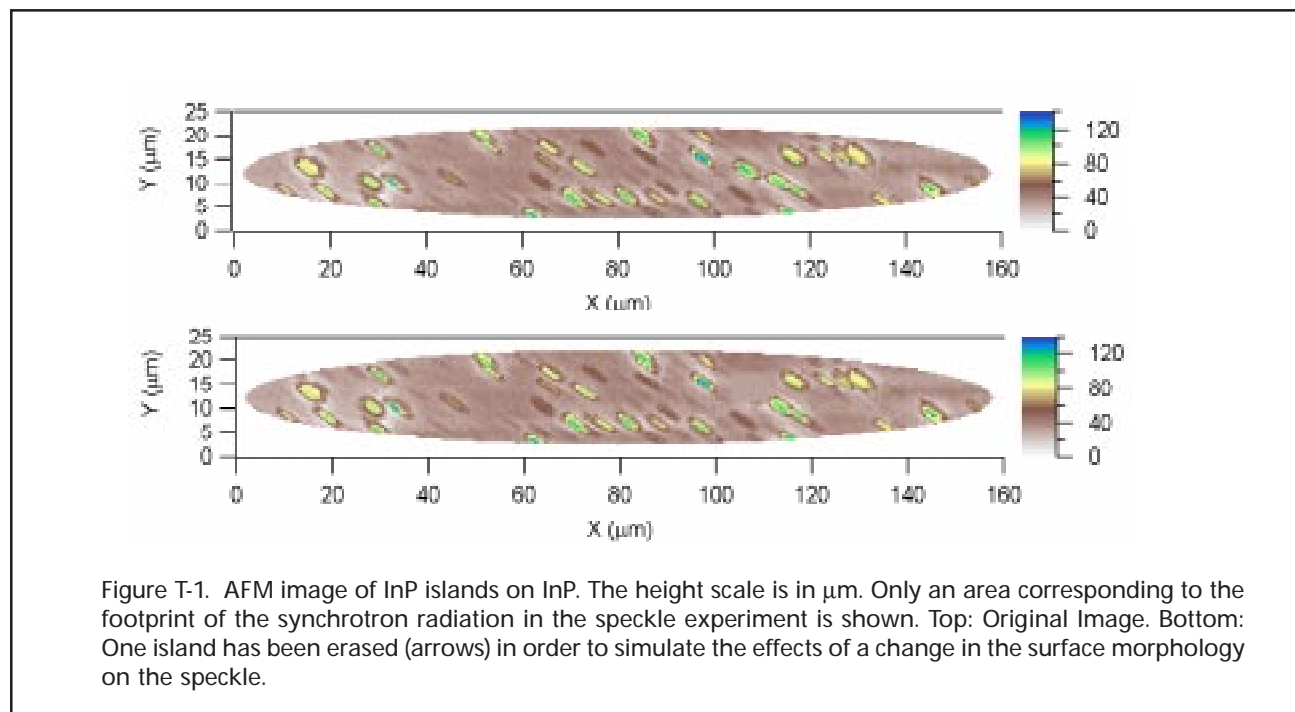# Soft X-Ray Speckle and Surface Morphology

S. Eisebitt, A. Karl, R. Scherer, and W. Eberhardt
(Institut für Festkörperforschung)
M. Adamcyk, C. Nicoll, T. Pinnington, and T. Tiedje
(U. of British Columbia, Advanced Materials and Process Engineering Lab.and
Department of Physics and Astronomy)

When coherent light scatters from a random surface, the intensity of the scattered light can exhibit a pronounced random interference effect known as speckle. The speckle pattern contains information on the particular configuration of the surface structure. This is in contrast to the scattering of incoherent light which measures statistical averages of the surface structure only. The time dependence of the speckle is the basis for the technique known as dynamic light scattering, which can provide information on surface diffusion and other dynamical effects in equilibrium systems. The spatial resolution for the structural information is limited by the wavelength of the light: shorter wavelengths improve resolution.

In the visible photon energy range, coherent light scattering has been successfully used for some time to study the dynamical properties of liquids and surface adsorbed species[1]. Some experiments have been carried out using hard X-rays in transmission[2] or reflection[3-5]. With measurements at the NSLS X1B beamline, we have recently demonstrated the feasibility of speckle experiments using soft x-rays[6]. In contrast to hard x-rays, the soft x-ray range has the advantage that the reflection coefficients of the samples are much higher. As a result, a wider range of scattering geometries is accessible while surface sensitivity is still retained.

Here, we report on the measurement of soft x-ray

Figure T-1. AFM image of InP islands on InP. The height scale is in μm. Only an area corresponding to the footprint of the synchrotron radiation in the speckle experiment is shown. Top: Original Image. Bottom: One island has been erased (arrows) in order to simulate the effects of a change in the surface morphology on the speckle.

speckle patterns from InP islands grown on InP with an InAs wetting layer. Numerical simulations of the partially coherent scattering have been carried out according to Huygens-Fresnel scattering theory in the Fraunhofer approximation, in order to understand the observed speckle patterns. The experiments were carried out at the X1B undulator beamline. To increase the lateral coherence length of the incident X-ray beam, the synchrotron radiation was apertured using a 20 μm pinhole. To ensure a sharp illuminated area on the sample, the downstream pinhole to sample distance was kept small (3 cm). The angle of incidence of the synchrotron beam on the sample can be varied, here we present data for 7.4° angle of incidence using 266 eV radiation. A movable position sensitive soft x-ray detector was placed typically 54 cm away from the sample. The detector is a microchannel plate stack with a 2D spatially resolving resistive anode readout. The active area is composed of 1024 x 1024 pixels, which are 40 μm x 20 μm in size.

The sample investigated consists of InP islands grown on InP by solid source molecular beam epitaxy. The surface morphology was investigated by RHEED and laser light scattering during growth and ex situ by atomic force microscopy (AFM). An AFM image of the InP islands is presented in **Figure T-1**. The image has been clipped with an elliptical pupil function in order to show the footprint of the incident soft x-rays on the sample. The surface morphology as measured by AFM has been used to simulate the speckle pattern. Details of the calculations are reported elsewhere[7]. Intuitively, the calculation can be envisioned in terms of summing the complex phase factors arising from the path difference between each point on the sample and the considered pixel on the detector. The finite lateral coherence length was determined by the simulation of measured Fraunhofer diffraction rings and taken into account in the speckle simulations. At the present stage, calculations were carried out assuming infinite longitudinal coherence, although we expect the longitudinal coherence length to be

$$L_{long} = \frac{\lambda^2}{\Delta\lambda} \approx 50\mu m$$

The measured speckle pattern of the InP sample using 266 eV photons along with the simulations are presented in **Figure T-2**. As indicated by the momentum transfer scales, the images were recorded/calculated symmetrically around the specular beam. For comparison, all three results are plotted on the same logarithmic colorscale, which is set by the dynamic range of the measured data. In order to study the effects of the beam coherence, the simulation in the middle panel includes the finite lateral coherence, while the simulation in the top panel assumes infinite coherence lengths.
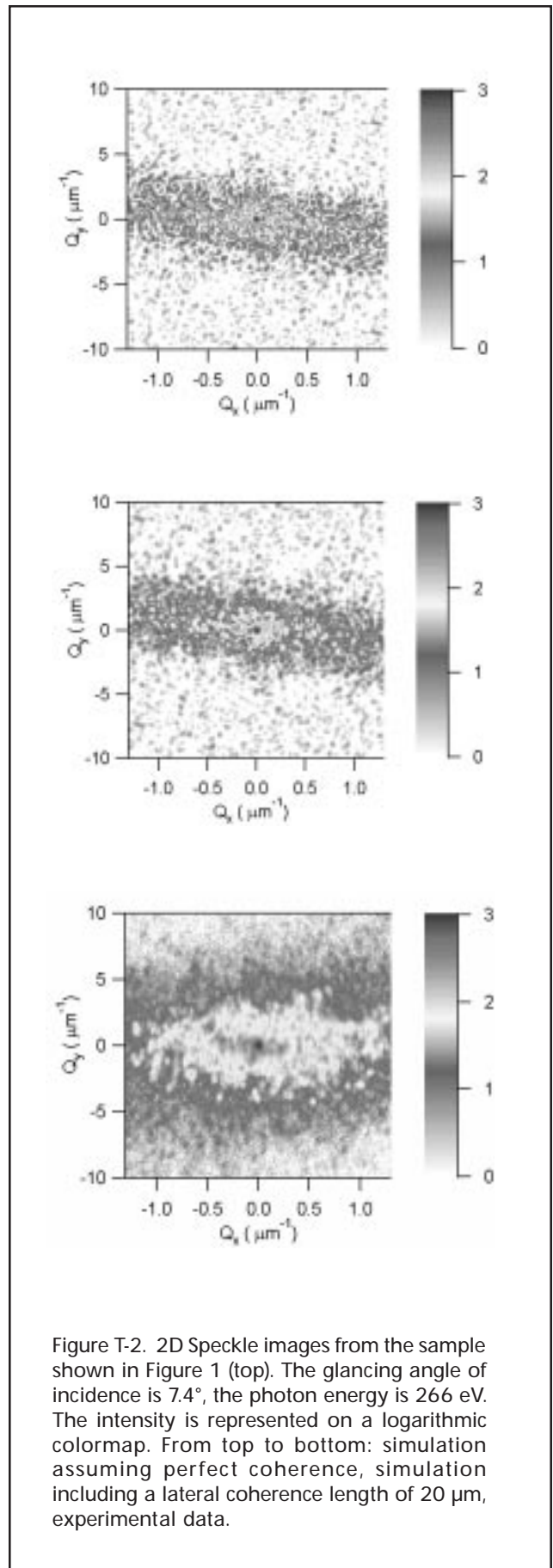

Figure T-2. 2D Speckle images from the sample shown in Figure 1 (top). The glancing angle of incidence is 7.4°, the photon energy is 266 eV. The intensity is represented on a logarithmic colormap. From top to bottom: simulation assuming perfect coherence, simulation including a lateral coherence length of 20 μm, experimental data.

The simulations reproduce the main features in the experimental data. The overall elongated shape of the intensity and the size of the speckles agree with the experiment. Of course, quantitative agreement of the speckle structure cannot be expected, as the AFM and speckle experiments are likely to probe different sample areas. As expected, the simulations illustrate that a reduction in the coherence of the synchrotron radiation results in a loss of contrast. With regard to the dynamic range, the agreement between experimental data and the simulation including the lateral coherence is good, but not perfect. We ascribe this discrepancy mainly to the influence of the longitudinal coherence, which is of the order of the maximum path difference between light beams scattered from either end of the illuminated region on the sample.

The distribution of the simulated x-ray scattering is tilted with respect to the frame of the image. This is caused by the orientation of the InP islands on the sample. In **Figure T-1** (top), the islands are elongated and are aligned with the [100] crystal direction on the substrate. The orientation of the islands creates the preferential scattering responsible for the tilt in the image. We observe a tilt in the same direction but with a smaller slope in the experimental data (especially when analyzing images at larger Q_x (not shown)) , which indicates that the alignment of the sample crystal axes was slightly off with respect to the plane of incidence.

The effect of a change in the surface morphology on the speckle pattern was evaluated by erasing one InP island from the AFM image used to simulate the scattering. The missing island is indicated by an arrow on both images in **Figure T-1**. The scattering simulation was computed with the modified AFM image and the resulting speckle pattern was subtracted from the original simulation. The absolute value of the difference image is shown in **Figure T-3** using the same logarithmic gray scale as in **Figure T-2**. There is a clear difference between
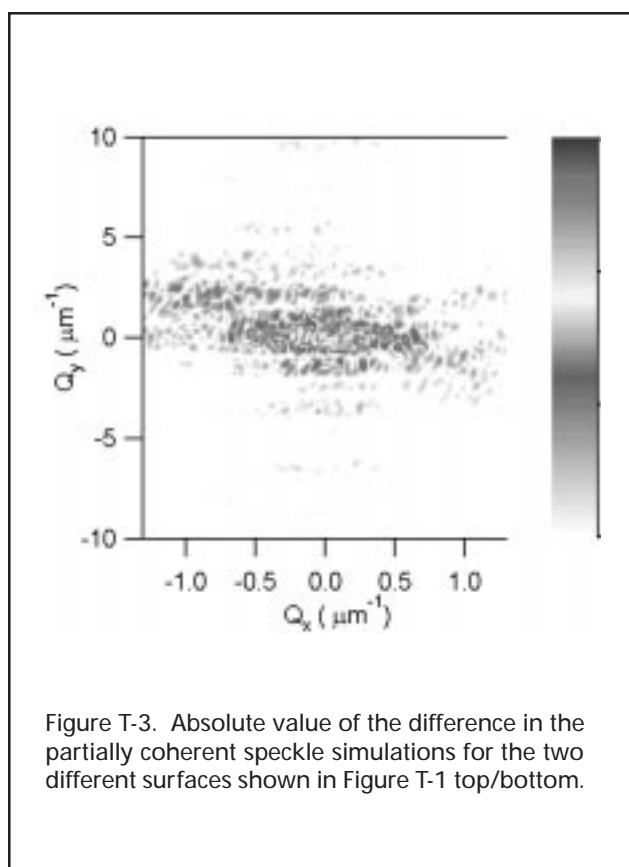

Figure T-3. Absolute value of the difference in the partially coherent speckle simulations for the two different surfaces shown in Figure T-1 top/bottom.

the two simulated speckle patterns, indicating that the soft x-ray speckle experiment is promising for the study of system dynamics. There are about 20 islands in the original AFM image which are responsible for the scattering. The removal of one island should therefore decrease the scattering by about 5% which is consistent with the difference image in **Figure T-3**: at the specular position, the intensity difference is about 1.3 orders of magnitude (i.e. a factor of 20) smaller than the intensity of the scattering. With a fast detector, which measures the intensity at one point only, studies of the dynamics at surfaces or buried structures will become possible. ■

REFERENCES

[1] See e.g. *Laser speckle and related phenomena*, Ed.J.C. Dainty, (Springer, Berlin, 1984).

[2] S. Brauer, G.B. Stephenson, M. Sutton, R. Brüning, E. Dufresne, S.G.J. Mochrie, G. Grübel, J. Als-Nielsen, and D. Abernathy, *Phys. Rev. Lett.*, **74**, 2010, (1995).

[3] Z.H. Cai, B. Lai, W.B. Yun, I. McNulty, K.G. Huang, and T.P. Russell, *Phys. Rev. Lett.*, **73**, 82, (1994).

[4] M. Sutton, S.G.J. Mochrie, T. Greytag, S.E. Nagler, L.E. Berman, G.A. Heald, and G.B. Stephenson, *Nature,* **352,** (1991).

[5] J.L. Libbert, R. Pindak, S.B. Dierker, and I.K. Robinson, *Phys. Rev. B*, **56,** 6454, (1997).

[6] S. Eisebitt, A. Karl, R. Scherer, W. Eberhardt, M. Adamcyk, T. Tiedje, and C. Pistonesi, *Synch. Rad. News* **11**, No. 5, p. 15, (1998).

[7] M. Adamcyk, T. Tiedje, S. Eisebitt, A. Karl, R. Scherer, W. Eberhardt, Proceedings of the 26th Conference on the Physics and Chemistry of Semiconductor Interfaces, to be published (1999).

A New Method for Examining the Dynamics of Macromolcules:Time-resolved Synchrotron X-ray "Footprinting"

M. Chance, M. Brenowitz, M. Sullivan, B. Sclavi, S. Maleknia, and C. Ralston (Center for Synchrotron Biosciences, Department of Physiology and Biophysics and Department of Biochemistry, Albert Einstein College of Medicine of Yeshiva U., and NSLS)

A new method of determining structure is under development at the National Synchrotron Light Source (NSLS) called synchrotron x-ray foootprinting. The goal is to probe the conformational dynamics and tertiary structure changes of proteins and nucleic acids with millisecond time resolution. This activity is being undertaken by the Albert Einstein College of Medicine and funded by NIH as a Biotechnology Resource Center. The technique of synchrotron x-ray footprinting is a melding of stopped-flow mixing technology and radiolytic chemistry using a high flux x-ray source. Radiolysis generates •OH according to equation 1:

$$H_2O \xrightarrow{h\nu} H_2O^+ + e^-_{dry} \xrightarrow{H_2O} H_3O^+ + \; \bullet OH \; + \; e^-_{aq} \qquad (1)$$
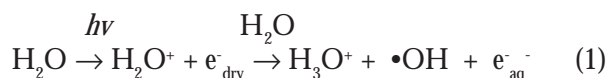
As photons interact with water and generate a water ion and an electron. The ionized water molecules react with water to produce •OH according to the reaction outlined in eq. (1). The kinetics and dose of •OH and its use in footprinting studies has been extensively reviewed[1,2].

The prediction underlying synchrotron x-ray footprinting is that irradiation of solutions by high flux "white light" x-ray beams at National Synchrotron Light Source (NSLS) beamline X9A yields sufficient concentrations of •OH so that footprinting studies of nucleic acids and proteins can be conducted with millisecond exposures to the x-ray beam. **Figure T-4** shows the flux emanating from a bending magnet port (impinging on a sample typical for a synchrotron footprinting experiment) at the NSLS when the ring
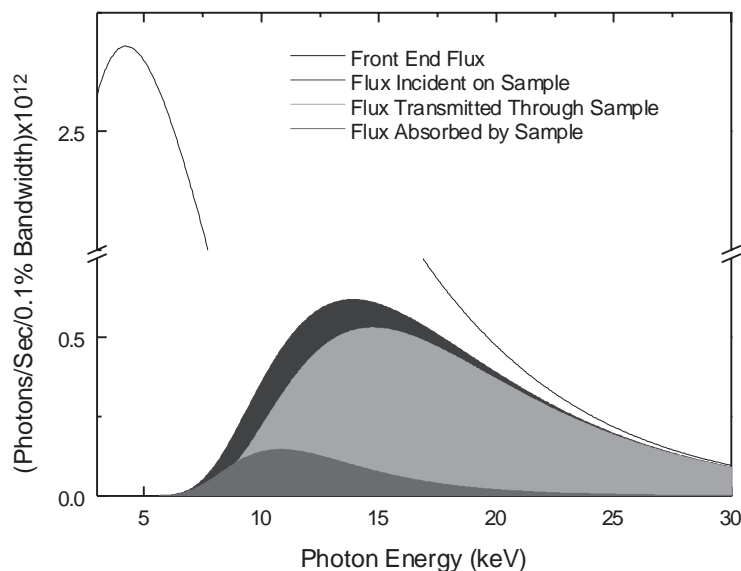

Figure T-4. Photon flux intercepted by a 1-mm pathlength sample of ~10 microliters (3-4 mm diameter) at beamline X9A, National Synchrotron Light Source. Beam energy of 2.54 GeV, 250 mA beam current. The figure indicates the front-end flux available for the specified geometry, the flux absorbed by the beamline optics incident on a typical sample, the flux passing through and absorbed by the sample.
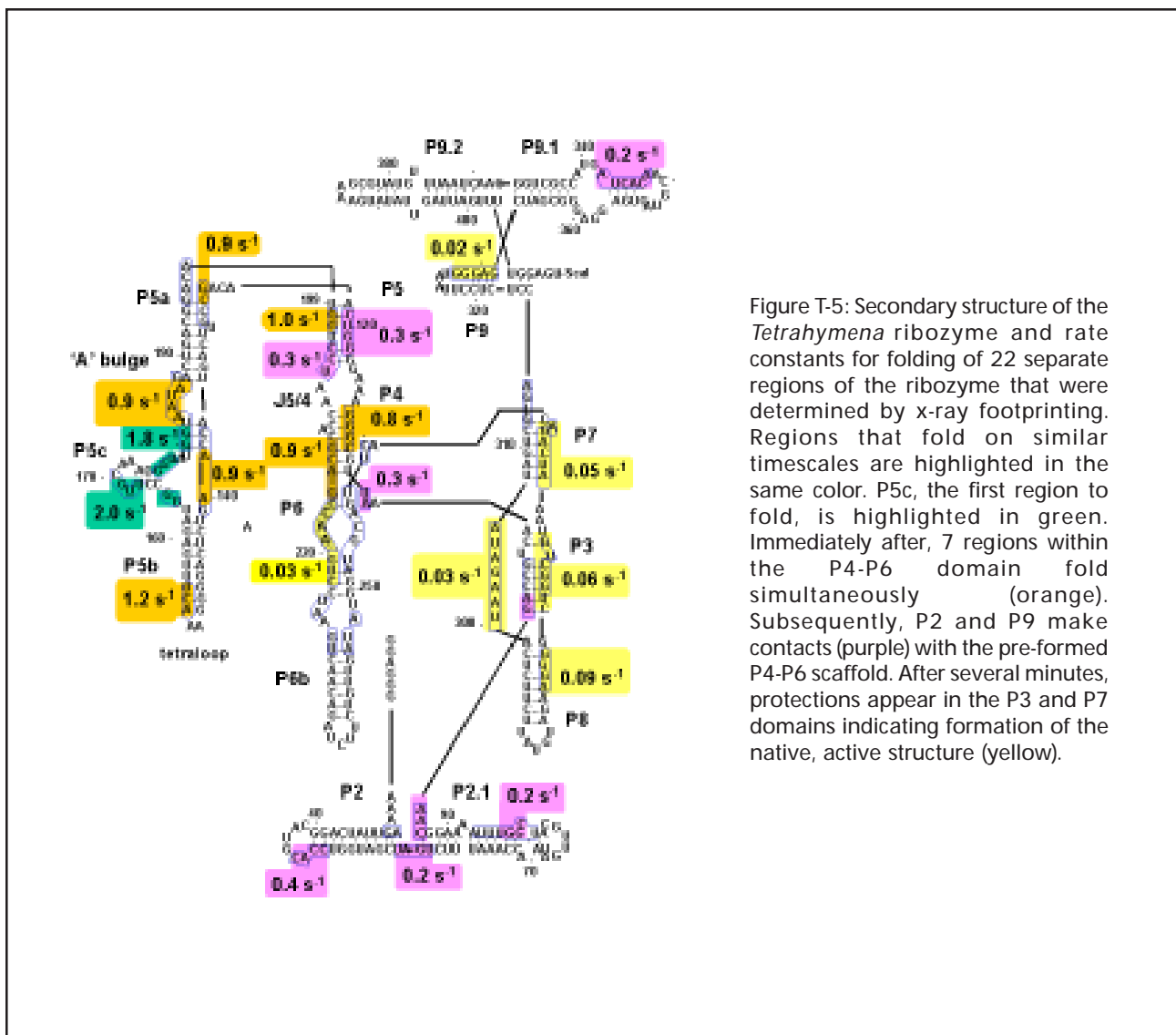
Figure T-5: Secondary structure of the *Tetrahymena* ribozyme and rate constants for folding of 22 separate regions of the ribozyme that were determined by x-ray footprinting. Regions that fold on similar timescales are highlighted in the same color. P5c, the first region to fold, is highlighted in green. Immediately after, 7 regions within the P4-P6 domain fold simultaneously (orange). Subsequently, P2 and P9 make contacts (purple) with the pre-formed P4-P6 scaffold. After several minutes, protections appear in the P3 and P7 domains indicating formation of the native, active structure (yellow).

energy is 2.54 GeV, as a function of energy. Taking into account losses due to the current beamline X9A optics, which consist of two Be windows (254 µ and 500 µ) and an Al window (200 µ), gives the flux incident on a typical 10 microliter sample as a function of energy. We can also calculate the transmitted flux subsequent to the 1-mm water path, the difference between the two curves is of course the absorbed dose. Note that total absorbance is small, thus the dose is homogeneously delivered through the 1-mm path.

Our first "proof of principle" of the method consisted of an analysis of the folding of an RNA catalyst, the *Tetrahymena* ribozyme[3]. During the folding of both proteins and RNA, dramatic changes in solvent accessibility occur. The conformation changes of RNAs in fact, can limit the speed of chemical reactions carried out by RNA catalysts[3]. As a result, the process by which

RNA molecules fold into their native conformation has received much attention. Early investigations into the folding of tRNA established approximate timescales for the formation of secondary (10^{-4}- 10^{-5} s) and tertiary interactions (10^{-2} - 10^{-1} s), with reorganization of incorrect secondary structure occurring more slowly (0.1 - 1 s)[4]. Recent work has shown that folding of large RNAs is more complex, involving multiple pathways[5,6]. Individual domains of an RNA may form at rates that differ by orders of magnitude, with some transitions requiring minutes to reach completion. Our synchrotron footprinting method, with the ability to monitor changes in the solvent accessibility throughout the RNA and monitor processes occurring from milliseconds to minutes, is ideally suited to investigate the complex folding of large RNAs.

The 385 nt. ribozyme derived from the *Tetrahymena* group I intron (**Figure T-5**) folds into a well-defined

tertiary structure in the presence of Mg^{2+}, which is required for activity[4]. Biochemical and genetic methods have identified at least three domains of tertiary structure that, when separated, can re-associate to form the active ribozyme. A 160 nt domain containing paired regions P4-P6 folds independently[7,8], and its structure has been determined by x-ray crystallography[7]. The Mg^{2+}dependent folding kinetics of the ribozyme were quantitated by determining the changes in solvent accessibility of individual sites as a function of time after the addition of magnesium ions. A powerful advantage of the footprinting method is that changes in protection in sites throughout the ribozyme can be monitored in a single experiment. **Figure T-5** summarizes the kinetic determinations of folding for 22 separate regions of the ribozyme that show significant changes in protection upon addition of Mg^{2+}. The rapidly protected sites corresponded to nucleotides that are excluded from solvent by folding of the P4-P6 domain upon itself; the tertiary interactions within the domain are established in a concerted manner at a rate of about 1 s^{-1} at 42 °C (colored in orange). A subset of nucleotides in P5c (**Figure T-5**) were protected about twice as rapidly as other regions in the P4-P6 domain (colored in green). This region is a Mg^{2+}-rich subdomain suggesting that formation of a "metal ion core"

in P5a-P5c could serve as a nucleation site for additional tertiary structure formation. Other regions highlighted in **Figure T-5** show that tertiary contacts with the other domains of the ribozyme occur more slowly (colored in purple).

These synchrotron footprinting results yield a complete kinetic 'map' for the folding of the ribozyme allowing detailed questions about the folding mechanism to be answered for this and other large RNAs. The methods used for analysis of RNA structure are immediately translatable into examining the evolving protections that occur upon binding of proteins to both DNA and RNA, and experiments to probe such interactions in real time are underway. The footprinting of proteins, to examine the time-resolved changes in protection of a protein molecule, either in a folding reaction or in macromolecular assembly processes, is also being addressed through synchrotron applications. Although detailed discussion of the technical challenges of these applications are beyond the scope of this article, the modification of proteins by hydroxyl radical occurs on timescales equivalent to those of nucleic acid cleavage, use of advanced analytical techniques, like mass spectrometry can monitor these modifications and provide new probes of macromolecular structure[9,10]. ■

REFERENCES

[1]   B. Sclavi, S. Woodson, M. Sullivan, M.R. Chance, and M. Brenowitz, *J. Mol. Biol.,* **266**, 144, (1997), and B. Sclavi, M. Sullivan, M. Chance, M. Brenowitz, and S.A. Woodson, *Science,* **279**, 1940, (1998).

[2]   M.R. Chance, B. Sclavi, S.A.Woodson, and M. Brenowitz, *Structure,* **5**, 865, (1997) and B. Sclavi, S. Woodson, M. Sullivan, M. Chance, M. Brenowitz, *Methods in Enzymology,* **295**, 379, (1998).

[3]   T.R. Cech and D. Herschlag, *Nucleic Acids and Molecular Biology,* edited by F. Eckstein and D. M. J. Lilley, **10**, 1, (1996).

[4]   D.E. Draper, *Nature Struct. Biol.*, **3**, 397, (1996).

[5]   P.P. Zarrinkar, and J.R. Williamson, *Science,* 265, 918, (1994).

[6]   P.P. Zarrinkar, and J.R. Williamson, *Nature Struct. Biol.*, **3**, 432, (1996).

[7]   J.H. Cate, A.R. Gooding, E. Podell, K. Zhou, B.L. Golden, C.E. Kundrot, T.R. Cech, and J.A. Doudna, *Science,* **273**, 1678, (1996).

[8]   F.L. Murphy, and T.R. Cech, *Biochemistry* , **32**, 5291, (1993).

[9]   S.D. Maleknia, and M.R. Chance, Proceedings of the 46th Annual Conference on Mass Spectrometry and Allied Topics,Orlando, Florida, p. 972, (1998).

[10] S.D. Maleknia, S. Goldsmith, S. Vorobiev, S.C. Almo, M.R. Chance, and K.M. Downard, Proceedings of the 46th Annual Conference on Mass Spectrometry and Allied Topics, Orlando, Florida, p. 973 (1998).

High-Resolution X-Ray Fluorescence Spectroscopy at X25: Where are the Electrons? Who are the Ligands?

U. Bergmann, P. Glatzel and S.P. Cramer
(Lawrence Berkeley National Laboratory and U. of California at Davis)

A newly designed multi-crystal X-ray spectrometer is described and applications in the field of X-ray fluorescence spectroscopy are discussed. The instrument is based on 8 spherically curved crystals aligned in the Rowland geometry (see schematic setup in **Figure T-6**). Each crystal has three degrees of freedom for adjustment, Bragg angle, azimuthal angle and distance to the source and detector. The design is very flexible and crystals of different size and bending radius can be employed. If all crystals have the same distance to the source scans can be facilitated by moving the motorized spectrometer table to change all Bragg angles simultaneously.
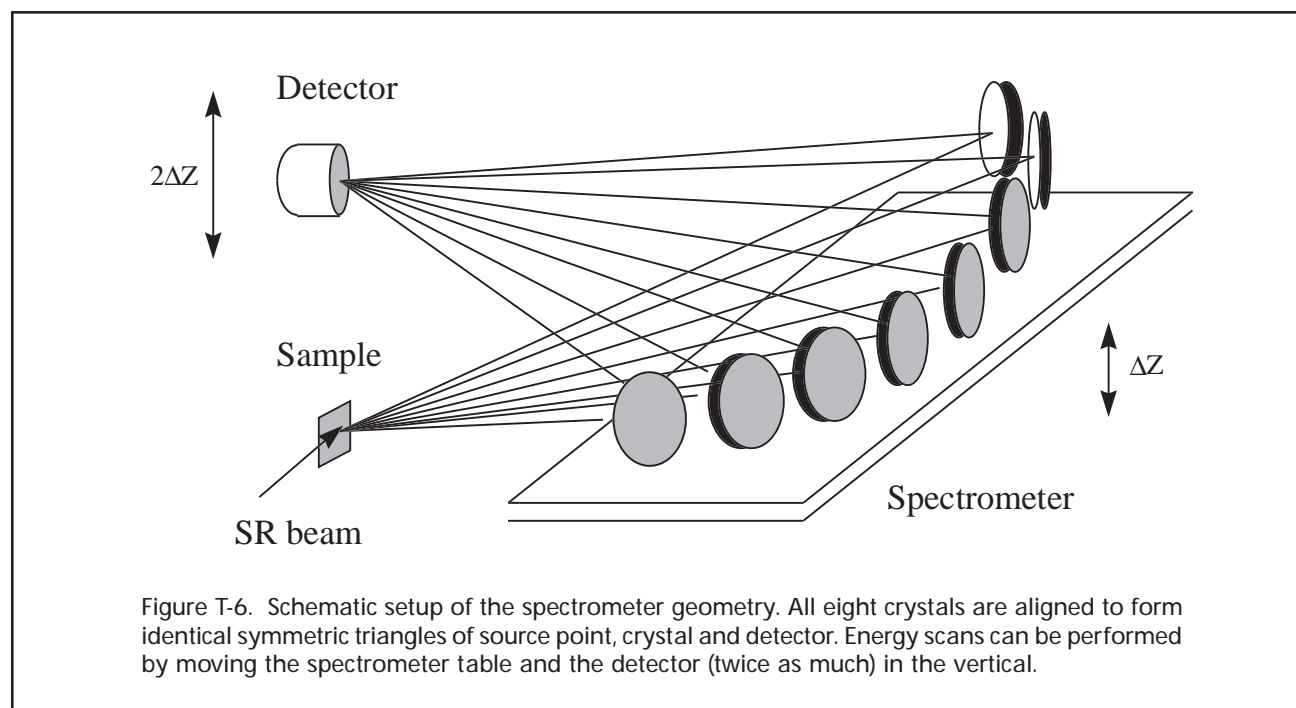
Currently eight 8.9 cm diameter Si (4,4,0) crystals bent to 86 cm radius are employed. At Bragg angles close to backscattering a solid angle of $1/180$ of the total 4π sr can be captured with sub eV energy resolution. To avoid intensity losses due to absorption on the long paths between source crystals and detector, a He-filled bag that encloses the entire beam path is inserted. An instrument combining such a large solid angle with high energy resolution is ideally suited for analysis of weak quasi isotropic signals. Among the many possible applications the technique of $K\beta$ fluorescence spectroscopy is illustrated with two examples.

WHERE ARE THE ELECTRONS?

It has been shown that the main lines of the $K\beta$ fluorescence $(3p \rightarrow 1s$ transition) in transition metals are strongly influenced in shape as well as energy by the number of unpaired 3d electrons. Hence $K\beta$ spectra give an excellent signature of the oxidation and/or spin state. Due to their variety of oxidation states, transition metals play an important role in catalytic processes. Obviously the knowledge the oxidation state is of fundamental importance for the understanding of these processes.

One predominant example of a catalytic process in nature is the oxidation of water in photosystem II, a mechanism responsible for essentially all the oxygen in our atmosphere. The catalytic center for this process is a cluster containing 4 Mn atoms. The oxygen is released

Figure T-6. Schematic setup of the spectrometer geometry. All eight crystals are aligned to form identical symmetric triangles of source point, crystal and detector. Energy scans can be performed by moving the spectrometer table and the detector (twice as much) in the vertical.

after the fourth step in the so called Kok cycle, in each of which a visible light photon had been absorbed.

In collaboration with the Penner-Hahn, Christou and Armstrong Groups, high resolution Mn Kβ X-ray fluorescence spectra have been recorded on the dark-adapted S_1 state and the hydroquinone-reduced of photosystem II [2]. By comparison of the Kβ chemical shifts with those of appropriate model compounds, the S_1 state is found to contain equal amounts of Mn(III) and Mn(IV). In the hydroquinone-reduced sample, a significant fraction of the Mn is reduced to Mn(II), and the results are compatible with models involving conversion of $Mn(III)_2Mn(IV)_2$ to $Mn(II)_2Mn(IV)_2$ clusters.

In a collaboration with the Klein Group at Calvin Lab, we have then studied the evolution of the Mn oxidation states through different S-states in the Kok cycle. Our preliminary findings are consistent with the Berkeley model of Mn(II,III,IV) for S_0, Mn(III$_2$,IV$_2$) for S_1 and Mn(III,VI$_3$) for both S_2 and S_3 states [3,4].

WHO ARE THE LIGANDS?

Besides the work on the very dilute protein samples, the large solid angle combined with the high incident flux at X25 enabled us to systematically study much weaker Kβ emission features appearing at higher emission energies (see **Figure T-7**). These transitions result from valence orbitals close to the Fermi level and, in some cases, even ligand orbitals. In particular we studied the so called "interatomic" or "crossover" x-ray transitions of ligand (N, O, F) 2s to metal (Mn) 1s [5], also known as Kβ".

The energy of the Kβ" feature is very distinct even for ligands of neighboring Z, resulting in shifts of order 5 eV. It can therefore be used to identify the type of ligand. Furthermore, for a variety of oxygen ligated Mn compounds, the intensity of the Kβ" transition is found to decrease exponentially with increasing Mn-O. The normalized Kβ" intensity can be used to predict distances to ~0.1 Å. The result demonstrates the potential of this technique as a new alternative to tell not only who but also where the ligands are. ■

REFERENCES

[1] U. Bergmann and S. P. Cramer, SPIE Proceedings, **3448,** 198-210 (1998).
[2] U. Bergmann et al., *J. Phys. Chem. B*, **102/42**, 8350-8352 (1998).
[3] J. Messinger et al., Proceedings of the XI. Int. Congress on Photosynthesis 1998, edited by J. Garab, Kluwer Academic Pub., The Netherlands, in press.
[4] R. M. Cinco et al., Proceedings of the XI. Int. Congress on Photosynthesis 1998, edited by J. Garab, Kluwer Academic Pub., The Netherlands, in press.
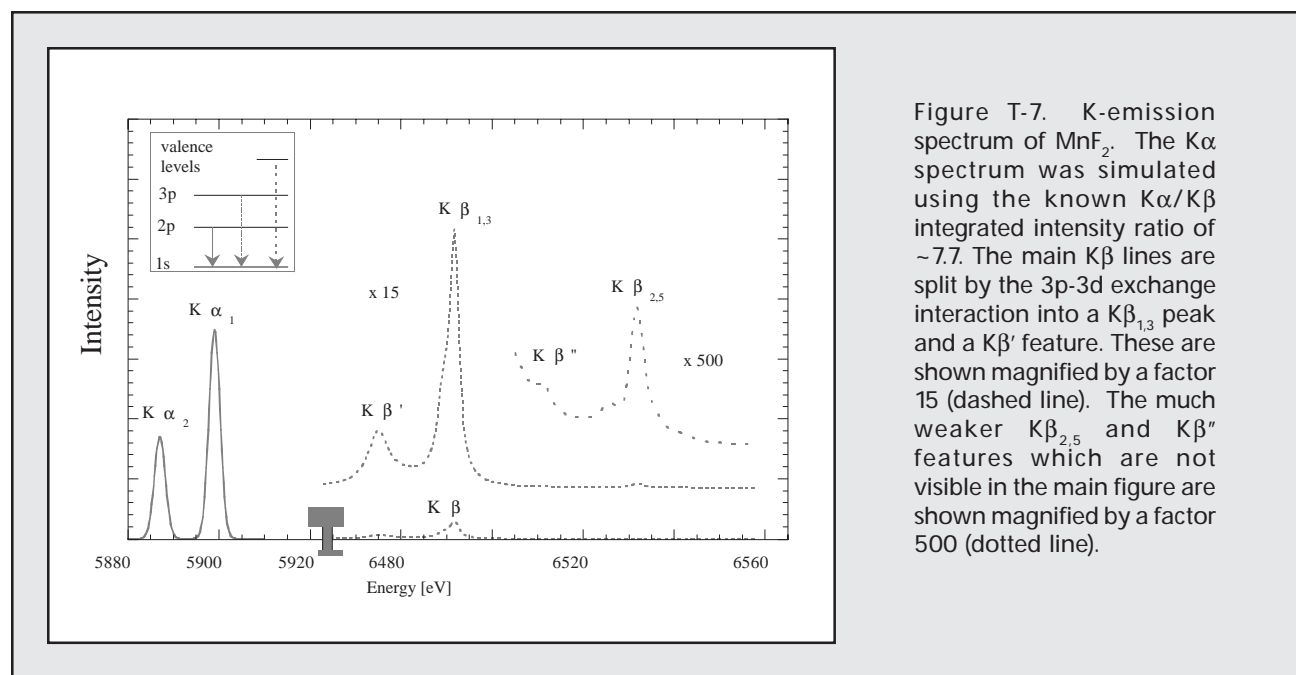[5] U. Bergmann et al., *Chem. Phys. Lett.*, accepted.

Figure T-7. K-emission spectrum of MnF$_2$. The Kα spectrum was simulated using the known Kα/Kβ integrated intensity ratio of ~7.7. The main Kβ lines are split by the 3p-3d exchange interaction into a Kβ$_{1,3}$ peak and a Kβ′ feature. These are shown magnified by a factor 15 (dashed line). The much weaker Kβ$_{2,5}$ and Kβ″ features which are not visible in the main figure are shown magnified by a factor 500 (dotted line).

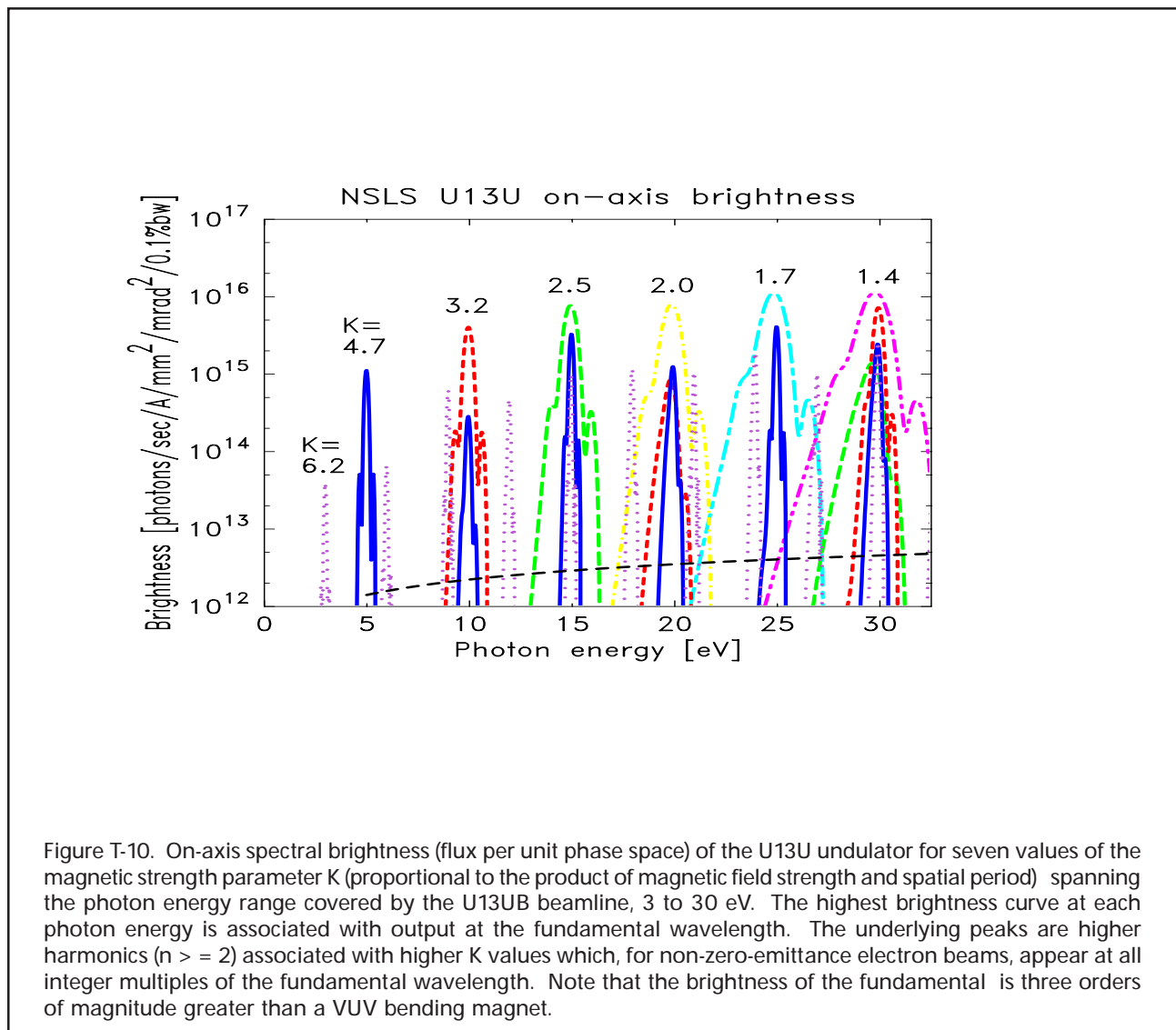# Newly Commissioned 3-30eV Undulator Beamline U13UB

S. L. Hulbert (NSLS), A. V. Fedorov, T. Valla, and P. D. Johnson (BNL Physics)

The low-K (undulator regime) output of the insertion devices on both NSLS storage rings is essentially "third generation", by being nearly diffraction-limited in one direction (vertical). As such, they represent an important and unique component of the synchrotron radiation facilities available in the U.S. The NSLS undulator sources are U5U and U13U in the VUV photon energy range and X1 and X13 in the soft x-ray range.

The brightness (flux per unit phase space) of the U13U undulator in the photon energy range covered by the U13UB beamline, 3 to 30 eV, is shown in **Figure T-10**. This figure plots the spectral brightness for seven values of the magnetic strength parameter K, for which the fundamental photon energy spans the 3 to 30 eV range. Note that the brightness of the undulator output is three orders of magnitude greater than a VUV bending magnet.

In terms of flux, the U13U undulator produces fundamental output greater than 2×10^{15} photons/sec/0.1%bandwidth/Amp in the 3-30 eV photon energy range. This range of fundamental photon energies $h\nu_1$ is readily achieved by changing the magnetic strength K from 4.7 to 1.4. The radiation is directed into a narrow spatial cone, e.g. the 1-σ opening angle is 210 µrad at $h\nu_1$ = 15 eV.

Figure T-10. On-axis spectral brightness (flux per unit phase space) of the U13U undulator for seven values of the magnetic strength parameter K (proportional to the product of magnetic field strength and spatial period) spanning the photon energy range covered by the U13UB beamline, 3 to 30 eV. The highest brightness curve at each photon energy is associated with output at the fundamental wavelength. The underlying peaks are higher harmonics (n > = 2) associated with higher K values which, for non-zero-emittance electron beams, appear at all integer multiples of the fundamental wavelength. Note that the brightness of the fundamental is three orders of magnitude greater than a VUV bending magnet.

This article focuses on the new U13UB beamline, which has been in operation since June 1998. The properties of the U13U source and the U13UB beamline are provided, followed by a general overview of the scientific opportunities which we envision for this beamline. Finally, a descriptive overview of two angle-resolved photoemission endstations destined for use at U13UB is given, including a sampling of the first experiments, which are ongoing.

COMPARISON WITH BENDING MAGNET SOURCE

In order to justify the use of a unique resource such as the U13U insertion device, is it necessary to show that a NSLS VUV bending magnet beamline could not produce the desired flux density at the sample. The flux output of 1 μrad horizontal of an NSLS VUV bending magnet is approximately 1×10^{13} photons/sec/0.1%bandwidth/Amp, and the vertical opening angle of radiation in the 3-30eV photon energy range is 5-10 mrad. In order to compete with U13U in terms of raw flux, a bending magnet beamline must collect a large horizontal fan, e.g. NSLS U11 collects 55 mrad in the horizontal plane.

However, such a beamline is saddled with problems related to the large phase space area of the bending magnet source (horizontally, vertically, and in depth). Clever optical designs, such as the modified Wadsworth monochromator at U11, provide fairly good energy resolution, but at the expense of providing a rather large focal "spot" (1 mm). The transverse (horizontal and vertical) phase space volume of the U13U radiation is on

the order of 250 to 500 times smaller than that of U11, which enables U13U to provide significantly higher flux density at the sample.

From this discussion, it is clear that the experiments which will benefit the most from the high brightness undulator beam at U13UB are those for which flux density on the sample defines the figure of merit. This class of experiments includes all of angle-resolved photoemission spectroscopy (ARPES), for example, since the electron energy analyzer in these experiments can accept emission from only a finite area on the sample. Further, as the energy resolution of these analyzers is improved, the size of this acceptance spot decreases dramatically.

U13UB BEAMLINE DESCRIPTION

Beamline U13UB is one of three branch beamlines which share the output of the U13U NdFeB hybrid wiggler/undulator (0.5 < K < 7.6) insertion device on the VUV Ring. The other two branches are U13UA, a focused white light beamline, and U13UC, a coherent optics characterization beamline. **Figure T-11** is an elevation layout drawing of the U13UB beamline, which was constructed by McPherson, Inc. of Chelmsford, MA.

The U13UB beamline is separated from the U13U centerline by a horizontally-deflecting (12° grazing angle of incidence) variable-radius (50m < R < 200m) integrally-water-cooled spherical mirror (M0B), which collects 1.66 mrad and focuses on the exit slit of the U13UB monochromator. The M0B mirror material is glidcop (ceramic copper alloy) explosion-bonded to a stainless steel substrate. The second optical element is a vertically-
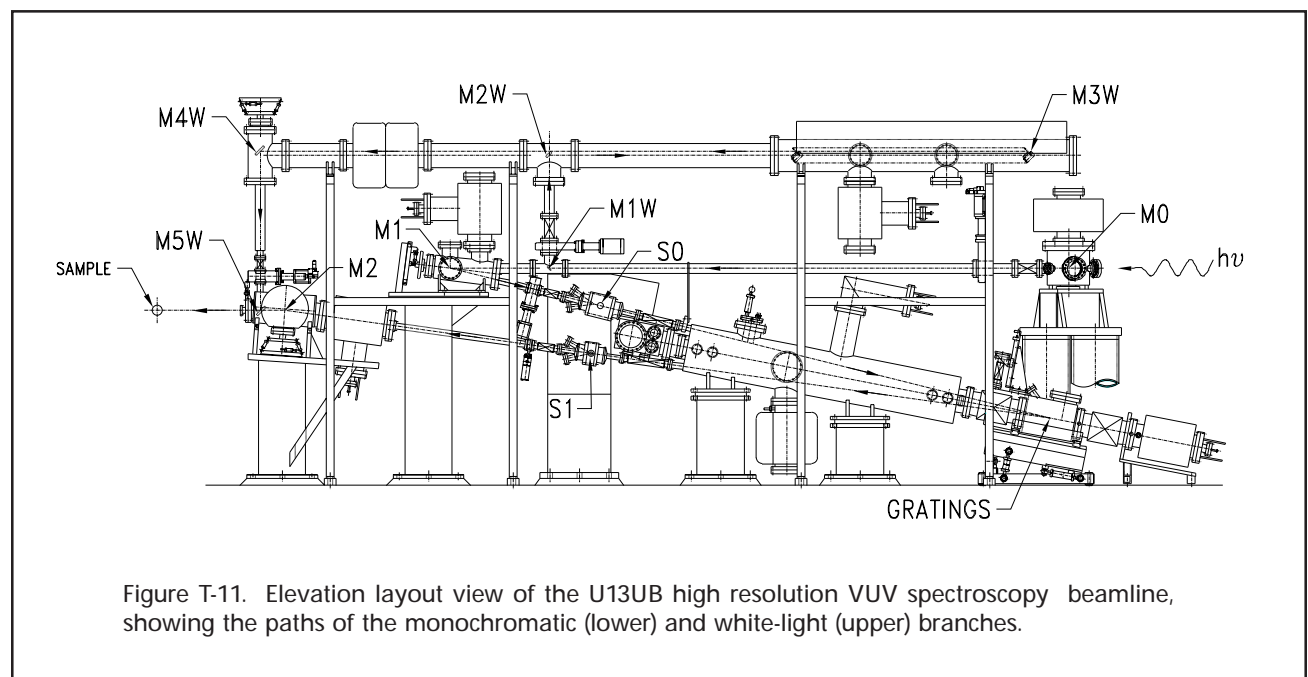

Figure T-11. Elevation layout view of the U13UB high resolution VUV spectroscopy beamline, showing the paths of the monochromatic (lower) and white-light (upper) branches.

deflecting (7° angle of incidence — nearly normal incidence) integrally-water-cooled spherical (R = 1.9m) mirror (M1B), which collects 2.4 mrad and focuses (with ~15:1 demagnification) on the entrance slit (S0B) of the monochromator. The large total output power (287W at K = 8, 500mA ring current) and significant output power densities (up to 32.5W/mrad^2 at K = 8, 500mA ring current) require water cooling of M0B, M1B, and S0B. Owing to its nearly normal incidence geometry, the lion's share of the source power is absorbed by the M1B mirror. The M1B mirror is a one-inch thick piece of CVD SiC and is integrally water cooled: finite element calculations show that the temperature rise, stress, and resulting deformation are well within the mechanical limits of this material (in fact they are all small).

The U13UB beamline features a Normal Incidence Monochromator (NIM) in which a spherical (R = 3m) grating is used in fixed included angle geometry. The grating chamber houses two gratings on a rotating turret with detents to select either of the two gratings *in situ*. These two gratings (1200 and 2400 line/mm

groove densities), and the ~3m entrance and exit armlengths in this monochromator, produce >10,000 spectral resolving power in overlapping photon energy ranges spanning 3 eV to 30 eV. The entire grating housing moves, under interferometric control, along the angle bisector between the entrance and exit beams, in order to track the photon energy-dependent focus of the diffracted exit beam. The grating angle scanning motion is provided by a DC servo system, also under interferometric control. The variable radius of the M0B mirror can be used to correct for the photon-energy-dependent astigmatism of the NIM as it scans through the 3-30 eV range.

OVERVIEW OF SCIENTIFIC OPPORTUNITIES USING BEAMLINE U13UB

Several types of scientific programs could be expected to benefit greatly by instrumenting the U13U wiggler for high resolution VUV work in the 3 to 30 eV range. Perhaps the most obvious application in solid state physics is ultra-high resolution angle resolved photoemission. In cases where the states of interest lie
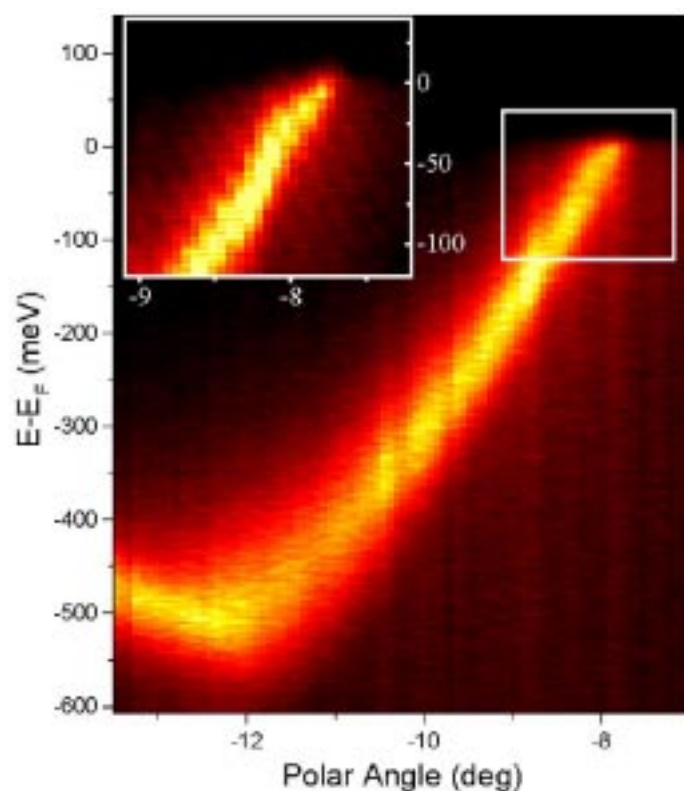

Figure T-12. ARPES intensity plot of the Mo(110) surface recorded along the $\overline{\Gamma}$ - $\overline{N}$ line of the surface Brillouin zone at 70°K. Inset: "fixed-mode"spectrum of the region around k_F (marked with box).

near the Fermi level, self-energy corrections are small, and reductions in the photon energy spread will significantly enhance the experiments. High T_c superconductors and heavy fermion systems are examples of such problems.

In addition, surface photo-voltage measurements, chemical dynamics applications, and photoelectron spectromicroscopy are all experiments for which spatial flux density is the relevant figure of merit, and could therefore be expected to be well matched to the U13UB beamline.

The section of beam pipe located vertically above the NIM beamline (see **Figure T-11**) houses relay optics which will provide a time-delayed (or advanced) white light beam, the focus of which will be collinear and coincident with that of the NIM beamline, for the purpose of pump-probe experiments. This capability is expected to be central to a large fraction of the biology experiments planned for U13UB.

ANGLE-RESOLVED PHOTOEMISSION ENDSTATIONS AND EXPERIMENTS

Angle-resolved photoemission, developed in the seventies, still represents the premier tool available for the study of the momentum dependence of the electronic structure in solids. Here the energy of the emitted photoelectron is measured as a function of the angle of emission. Combined with beamlines such as U13UB, a whole range of new electron spectrometers is expected to lead to a resurgence of activity in this area. By multiplexing in energy and angle, these new instruments allow a considerable reduction in data acquisition times. At the same time, they offer extremely high energy and momentum resolution. With these improvements, ARPES may be used to obtain direct access to the real and imaginary components of the electron self energy, a measure of the interaction of an electron or hole with its environment.

Two instruments are scheduled to exploit the high photon fluxes available from U13UB. The first is a 200 mm radius Scienta SES200 analyzer that has recently been commissioned in the group of Peter Johnson (Physics - BNL) and the second is a Gamma Data 50 mm radius spectrometer currently being constructed by Eric Jensen (Brandeis U.) and Kevin Smith (Boston U.).

Initial experiments using the SES200 have already been completed. An example is presented in **Figure T-12**, which shows a measurement of the dispersion of an electronic band in the vicinity of the surface of molybdenum[1]. Shown in more detail in the insert, the spectra clearly show a slight change in the rate of dispersion and a rapid narrowing of the band in the vicinity of the Fermi level. These changes are directly attributable to the interaction of the electrons with the lattice vibrations or phonons in this system.
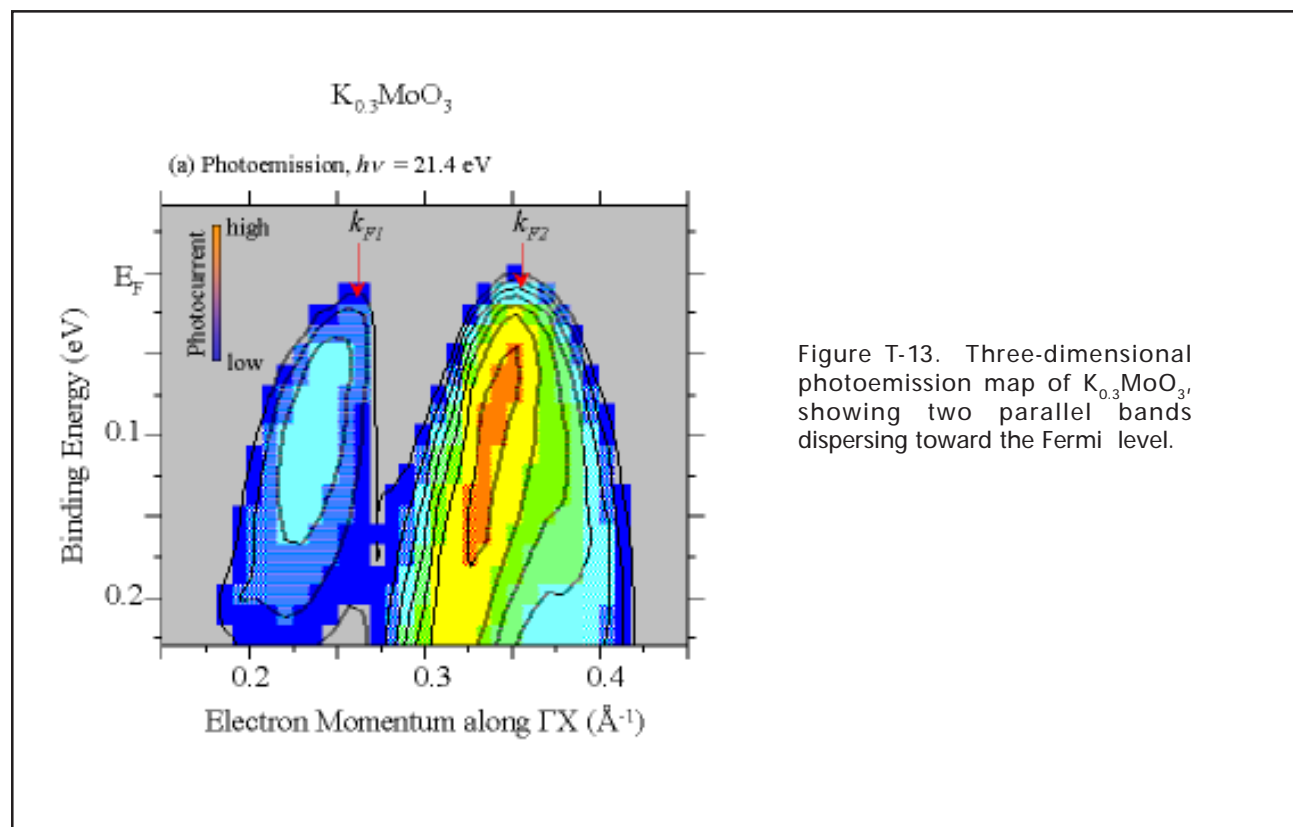

Figure T-13. Three-dimensional photoemission map of $K_{0.3}MoO_3$, showing two parallel bands dispersing toward the Fermi level.

Another example of the use of high momentum resolution is shown in **Figure t-13**. Here are shown the results of a study of the blue bronze, $K_{0.3}MoO_3$, which is a quasi-one-dimensional system having two chains per unit cell[2]. The valence electrons in this system form a charge density wave that results in a metal-semiconductor transition at 180°K. This study, carried out in collaboration with the Boston University Electronic Structure Group (K. Smith *et al.*), was able for the first time to clearly resolve two bands reflecting the interaction between the chains, as shown in **Figure T-13**. Furthermore, a detailed study of the temperature dependence of the wavevectors associated with these two bands provided a direct connection between the electronic structure and the temperature dependence observed for the wavevector of the charge density wave in this system.

As a final example of the new possibilities in ARPES, we show the results of a detailed temperature dependent study of optimally doped $Bi_2Sr_2CaCu_2O_8$ (BSCCO)[3]. These studies have found evidence for the opening of a gap in the spectral response with the onset of long range coherence at the superconducting transition temperature T_c. **Figure T-14** shows the emission from a region of momentum space when the sample is in the superconducting state. The "airplane wing" section corresponds to the superconducting paired electrons. **Figure T-15** shows temperature dependent "angle integrated" spectra obtained from images such as those shown in **Figure T-14**.

Figure T-15 shows that the sharp feature immediately below the Fermi level characterizing the superconducting state appears in the spectra even above the transition temperature T_c, 91°K, and that it remains at constant binding energy at all temperatures. Further, the spectra show that the intensity of this feature changes continuously on passing through T_c. This latter observation is surprising because within the framework of a mean field or BCS model, if the sharp peak reflects the super fluid density, it should disappear at T_c and, further, the separation between it and the Fermi level should disappear. However, the authors of the study, Fedorov, *et al.*, noted that at the transition temperature, a dip rapidly develops in the spectra immediately beyond the sharp peak. By fitting the angle-resolved data collected within an angle of 0.5°, Fedorov, *et al.* were able to show that the development of this dip may be associated with the opening of a gap at the Fermi level, reflecting the onset of long range phase coherence as defined by the transition temperature T_c. The latter development represents the extension of the pseudogap, which is reported to exist above T_c up to 130K in the optimally doped materials, to all states in the system. ∎
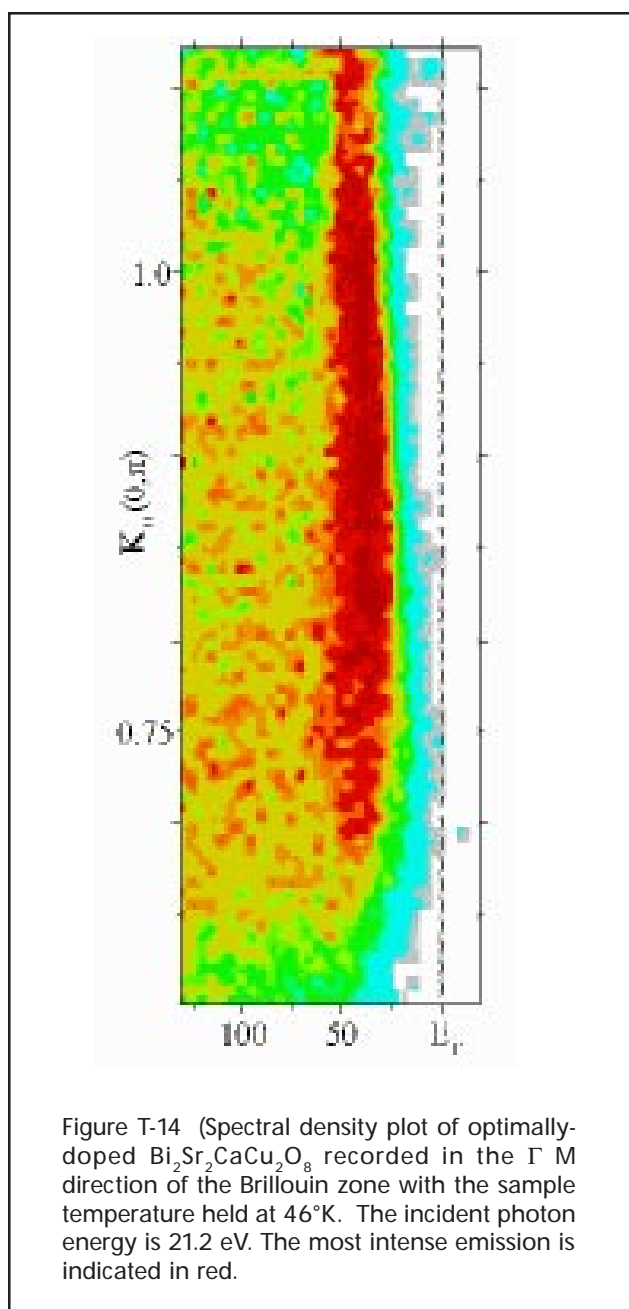

Figure T-14 (Spectral density plot of optimally-doped $Bi_2Sr_2CaCu_2O_8$ recorded in the Γ M direction of the Brillouin zone with the sample temperature held at 46°K. The incident photon energy is 21.2 eV. The most intense emission is indicated in red.
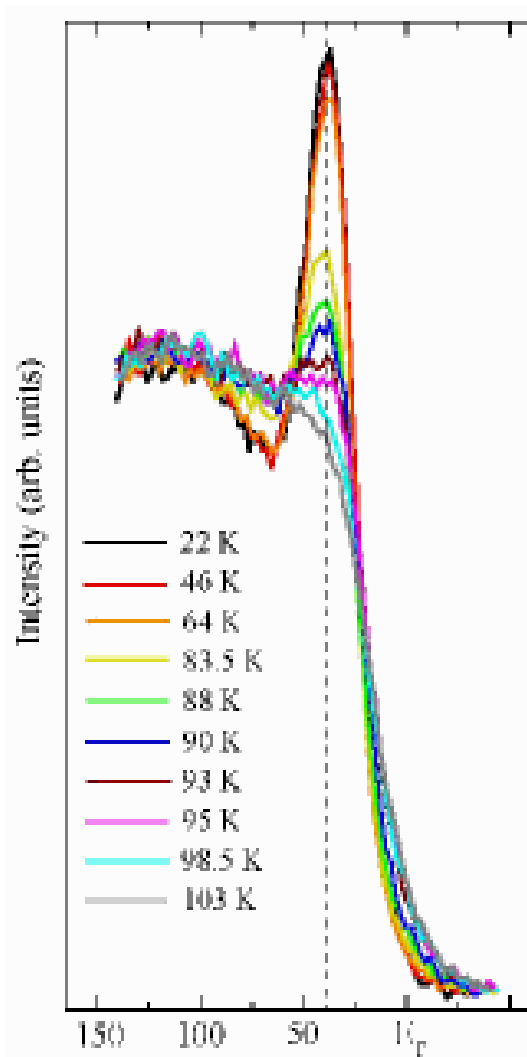
Figure T-15. Angle-integrated photoemission spectra of optimally-doped $Bi_2Sr_2CaCu_2O_8$ recorded as a function of temperature and integrated along the Γ M line of the Brillouin zone. The different temperatures are indicated.

REFERENCES

[1]   T. Valla, A. Federov, P. D. Johnson, and S. L. Hulbert, "Many-body Effects in Angle-resolved Photoemission: Quasiparticle Energy and Lifetime of the Mo(110) Surface State", *Phys. Rev. Lett.,* submitted (1999).

[2]   A. Federov, S. A. Brazovskii, V. N. Muthukumar, P. D. Johnson, J. Xue, L.-C. Duda, K. E. Smith, W. H. McCarroll, M. Greenblatt, and S. L. Hulbert, "Photoemission Study of the Charge Density Wave Transition in the Quasi-one Dimensional Conductor $K_{0.3}MoO_3$", *Phys. Rev. Lett.,* submitted (1999).

[3]   A. V. Fedorov, T. Valla, P. D. Johnson, Q. Li, G. D. Gu, N. Koshizuka, "Temperature Dependent Photoemission Studies of Optimally Doped $Bi_2Sr_2CaCu_2O_8$", *Phys. Rev. Lett.,* **82**, 2179, (1999).

A General Solution to the Diffraction Phase Problem in Systems with Two-Dimensional Periodicity

Y. Yacoby (Racah Institute of Physics, Hebrew U)
R. Pindak, R. MacHarrie and L. Pfeiffer,
(Bell Laboratories, Lucent Technologies)
R. Clarke (Randall Laboratory of Physics, U. of Michigan)
L. Berman (NSLS)

Material systems periodic in two dimensions and aperiodic in the third (2D crystals) are very interesting scientifically and often very important technologically. Crystal surfaces, crystals with epitaxially grown layers of another material, and interfaces, are all 2D crystals. They are scientifically interesting because physical and chemical phenomena at surfaces and interfaces are often different from those in the bulk, and are technologically relevant because many devices depend for their performance on material interfaces. Systems with an interface between a crystal and an amorphous material (e.g., Si and its oxide) are not ideal 2D crystals. However in the region of the interface, they do have partial two-dimensional periodicity. Finally, self-organized systems on crystalline surfaces are also 2D crystals and are currently of great interest both scientifically and technologically. Knowing the structure of these systems is crucial to understanding their properties and to the development of new processing techniques and devices.

Various x-ray methods have been used to investigate the structure of 2D crystals. These include reflectivity and diffuse scattering[1,2], high resolution x-ray diffraction[3], Multiple diffraction[4] and standing waves[5]. In all these methods, the structure cannot be directly determined. Instead it is necessary to first guess a structural model and then refine its parameters to obtain best fit with experiment. A step in overcoming this difficulty has been the development of a method to determine the layer structure using anomalous reflectivity[6].

In this paper we present a new x-ray method to determine directly the atomic structure of 2D crystals. We have successfully tested the method both in
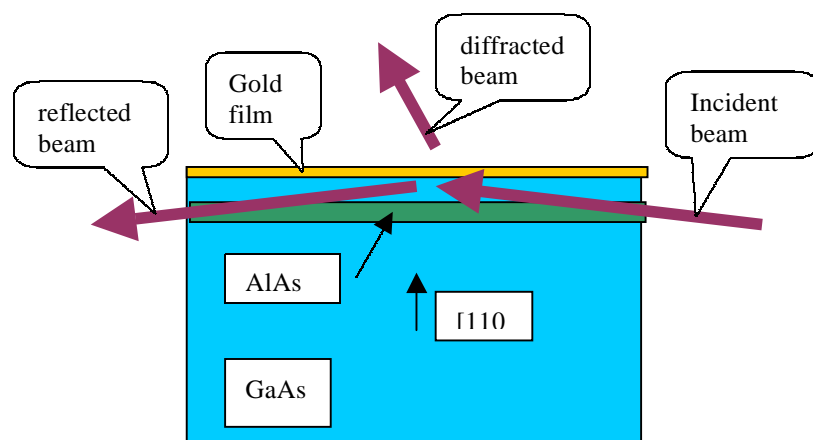

Figure T-16: Schematic diagram of the experiment. The sample consists of a GaAs crystal cleaved along the [110] plane. 4 monolayers of AlAs and 20 monolayers of GaAs were grown epitaxially on its surface. Two samples were prepared, with and without a 2000A gold overlayer. The gold film was used in order to measure the phase derivative along the Bragg rods as described previously[7,8].

simulations and in actual experiments. Using this method, we can determine the structure directly without the need to presuppose a structural model. As in all direct methods we measure not only the amplitude of the scattering factor but also its phase. The method we developed is general but it will be easier to explain using an example, shown in **Figure T-16**.

We consider a material system composed of a three-dimensional semi-infinite crystal with a known structure and a 2D crystal with an unknown structure. By definition, the 2D crystal is the difference between the whole system and the ideal 3D *semi-infinite* crystal. In our example, the 3D crystal is GaAs, extending all the way to the sample surface. The unknown 2D crystal is a few monolayers of epitaxial AlAs and its electron density is equal to the difference between the electron density of the ideal GaAs and that of the AlAs. Notice that if the GaAs is distorted relative to the ideal structure the difference will also show up in the 2D crystal representing the epitaxial AlAs and its interface with the GaAs.

The 3D crystal defines a 2D grid on planes parallel to its surface. At first we assume that the 2D crystal is periodic with respect to this grid. The complex scattering factor of the semi-infinite substrate crystal $S(k_z)$ is well-defined because its structure is known. However, the scattering factor of the 2D crystal $D(k)$, which will contribute to the scattering intensity along the Bragg rods, is not known. What is directly measured is the absolute value of the total scattering factor $|T|$ which is the absolute value of the complex sum of the two. We now consider two points along a Bragg rod at a small separation Δk_z from each other. Then,

$$S(k_z) + D(k_z) = |T(k_z)|e^{i\varphi(k_z)} \qquad (1)$$

$$S(k_z + \Delta k_z) + D(k_z + \Delta k_z)$$
$$= |T(k_z + \Delta k_z)|e^{i[\varphi(k_z) + \partial\varphi/\partial k_z \Delta k_z]} \qquad (2)$$

Here, $\varphi(k_z)$ is the unknown phase of T and $\partial\varphi/\partial k_z$ is the derivative of this phase along the Bragg rod. Notice that these equations cannot be solved for the complex scattering factor of the unknown crystal, $D(k)$ because $\varphi(k_z)$ is not known. We have recently developed, and experimentally demonstrated, a method to measure the phase derivative $\partial\varphi/\partial k_z$ along the Bragg rods[7,8]. In principle one could integrate the measured phase derivative in order to obtain the phase itself. The problem is that even a small amount of noise in the experimental data produces large errors in the phase, rendering the method useless. It was therefore necessary to find a way to use the phase derivative directly without the need to integrate.

In Eqs. 1 and 2 we have assumed that the real-space zero reference point of the x-ray dielectric function is at the sample surface. If this reference point is shifted in the z direction by z_0, Eqs. 1 and 2 will have the form:

$$S(k_z)e^{ik_z z_0} + D(k_z)e^{ik_z z_0} = |T(k_z)|e^{i\varphi(k_z)}e^{ik_z z_0} \qquad (3)$$

$$S(k_z + \Delta k_z)e^{i(k_z + \Delta k_z)z_0} + D(k_z + \Delta k_z)e^{i(k_z + \Delta k_z)z_0}$$
$$= |T(k_z + \Delta k_z)|e^{i[\varphi(k_z) + \partial\varphi/\partial k_z \Delta k_z]}e^{i(k_z + \Delta k_z)z_0} \qquad (4)$$

We now find a z_0 value such that

$$\Delta\overline{D} = |\overline{D}(k_z) - \overline{D}(k_z + \Delta k_z)| \qquad (5)$$

has a minimum. Here $\overline{D}(k_z) = D(k_z)e^{ik_z z_0}$. Notice that in this case the complex numbers $\overline{D}(k_z)$ and $\overline{D}(k_z + \Delta k_z)$ have the same argument. If $\Delta\overline{D}$ is at its minimal value, its absolute value will be in general small compared to $|\Delta\overline{S}|$ and $|\Delta\overline{T}|$ and can therefore be neglected. Then the absolute value of the difference between Eqs. 3 and 4 has the form:

$$|S(k_z + \Delta k_z)e^{i\Delta k_z z_0} - S(k_z)| =$$
$$|T(k_z + \Delta k_z)|e^{i\partial\varphi/\partial k_z \Delta k_z}e^{i\Delta k_z z_0} - |T(k_z)|| \qquad (6)$$

Notice that here all the values except for z_0 are known. So this equation can be used to determine z_0. We can now use the ratio between Eqs. 3 and 4 to determine $\overline{D}$.

$$\frac{\overline{S}(k_z + \Delta k_z) + \overline{D}}{\overline{S}(k_z) + \overline{D}} = \frac{|T(k_z + \Delta k_z)|e^{i(\partial\varphi/\partial k_z + z_0)\Delta k_z}}{|T(k_z)|} \qquad (7)$$

Where,

$$\overline{D} = D(k_z)e^{ik_z z_0} \cong D(k_z + \Delta k_z)e^{i(k_z + \Delta k_z)z_0} \qquad (8)$$

This procedure provides $D(k_z)$ for all relevant Bragg rods in reciprocal space. Back-Fourier transforming it in three-dimensions into real space, provides the 3D real space dielectric function $\varepsilon(\vec{\rho}, z)$. Here $\vec{\rho}$ is the position vector in the 2D unit cell and z is the distance in the direction normal to the plane of the 2D crystal.

It turns out that in many systems the value of z_0 can be estimated without measuring $\partial\varphi/\partial k_z$ along the Bragg rods. In systems where the thickness of the unknown 2D structure is small compared to its distance from the crystal surface, z_0 is approximately equal to this distance. In this case Eq. 6 can be used to determine $\partial\varphi/\partial k_z$ and Eq. 7 to determine the value of $\overline{D}$.

The method we developed is also applicable if the unknown 2D system is not fully periodic with respect to the 2D grid. It can be shown that in this case the exact same procedure provides an average complex dielectric function $\varepsilon(\vec{\rho}, z)$

$$\varepsilon(\vec{\rho}, z) = \frac{1}{N} \sum_j \varepsilon(\vec{\rho} + \vec{R}_j, z) \qquad (9)$$

Here, $\vec{\rho}$ is a position vector in the substrate-defined 2D unit cell; $\vec{R}_j$ is the 2D position of the jth unit cell, z is the distance from the nominal interface and the sum is carried over all 2D unit cells.

We have demonstrated this method experimentally using the system shown in **Figure T-16**. The diffraction profiles were measured along one Bragg rod from [-5 -1 1] to [1 5 1]. The data were then analyzed using the method discussed above, resulting in the complex scattering factor along the Bragg rod. This was then back-Fourier transformed in one dimension resulting in the Al density as a function of the distance from the crystal surface.

In **Figure T-17** we show the Al concentration as a function of the distance from the surface. The top curve represents the Al concentration obtained from simulated diffraction data calculated for the nominal sample used in the experiment. We included in this data noise and background typical of those we have in our experiments. The results are shown in curve (c). Each peak in the figure represents one monolayer. The distance between monolayers is 2Å, namely we have atomic resolution. Notice that the analysis indeed faithfully reproduces the initial structure.

Curves 2a and 2b represent the structure obtained from the analysis of the experimental data. Note that Al is present not only in the 4 monolayers that were intended as the AlAs 2D crystal, but also there is some Al concentration in one or two additional monolayers which were intended to be pure GaAs. On the other hand the structure of the cleaved crystal seen on the right of the AlAs layer has hardly been affected. It is also interesting to notice that the number of GaAs monolayers above the AlAs layer is different in the two samples in spite of the fact that the two samples were grown simultaneously but at two different places in the growth chamber.

It should be emphasized that the results shown in **Figure T-17** are from analyzing just one Bragg rod. Determining the complex scattering factor along all the relevant Bragg rods and back Fourier transforming the results in 3D will provide the positions of the various atoms in the 2D-unit-cell as a function of the distance from the surface.

In conclusion, we have demonstrated a method to experimentally determine the complex scattering factor along the Bragg rods of a 2D crystal. We have shown that using this data we can determine the structure of the 2D crystal by back-Fourier transforming the results. We expect that this method will be useful in the investigation of crystal surface structures, interfaces between a crystal and epitaxially grown layers, crystal-melt and crystal-solution, and self-ordered systems grown on a crystalline surface. The method can also be also used to investigate structural phase transitions at surfaces and interfaces. ∎
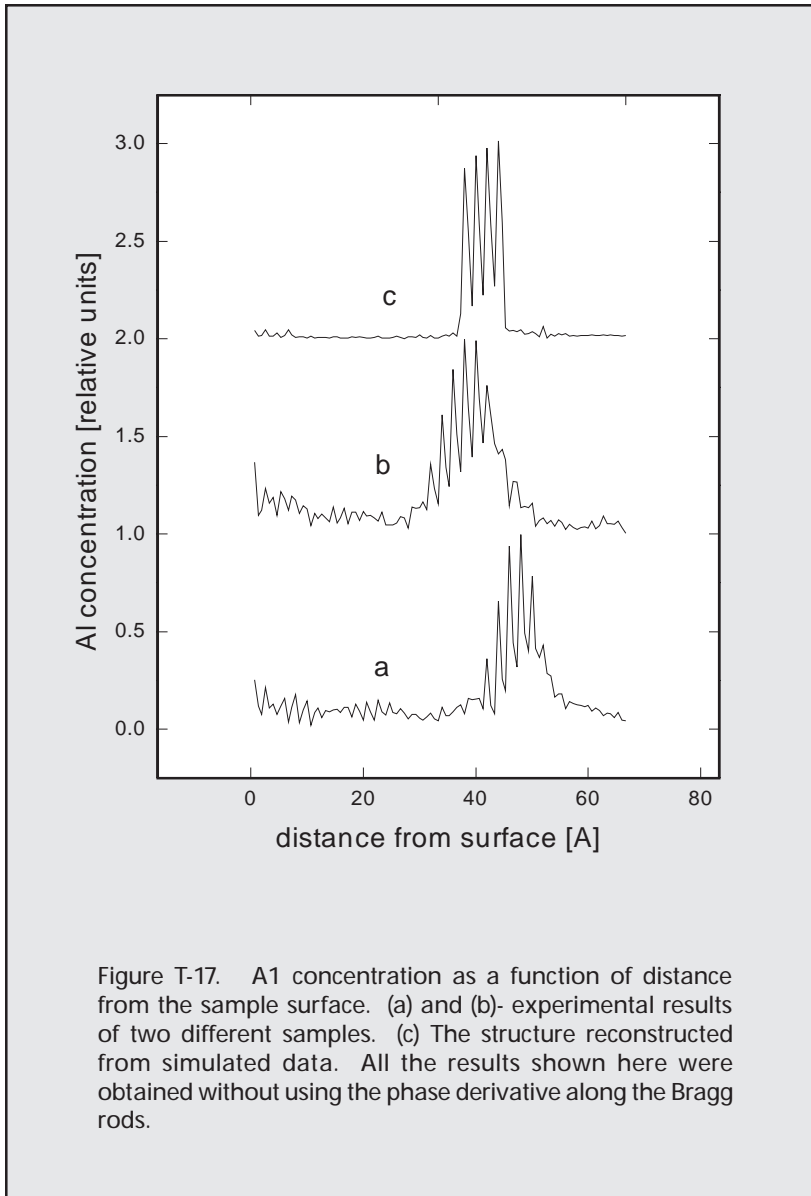

Figure T-17. A1 concentration as a function of distance from the sample surface. (a) and (b)- experimental results of two different samples. (c) The structure reconstructed from simulated data. All the results shown here were obtained without using the phase derivative along the Bragg rods.

REFERENCES

[1] S.K. Sinha, M.K. Sanyal, S.K. Satija, C.F. Majkrzak, D.A. Neumann, H. Homma, S. Szpala, A. Gibaud, and H. Morkoc, *Physica*, **B198**, 72, (1994).

[2] P.F. Miceli, <u>Semiconductor Interfaces, Microstructures and Devices: Properties and Applications</u>, edited by Z.C. Feng, IOP Publishing, Bristol UK, p. 87, (1993).

[3] I.K. Robinson and D.J. Tweet, *Reports on Progress in Physics*, **55**, 599, (1992).

[4] S.L. Morelhao and L.P. Cardoso, *J. of Appl. Phys.*, **73**, 4218, (1993).

[5] J. Zegenhagen, *Surface Science Reports*, **18**, 199, (1993).

[6] M. K. Sanyal, S. K. Sinha, A. Gibaud, et al., *Europhysics Letters*, **21**, 691, (1993).

[7] Y. Yacoby, *Solid State Comm.*, **91**, 529, (1994).

[8] H. Baltes, Y. Yacoby, R. Pindak, R. Clarke, L. Pfeiffer, and L. Berman, *Phys. Rev. Letters*, **79**, 1285, (1997).